Sulfur isotopic zoning in apatite crystals: A new record of dynamic sulfur behavior in magmas

Rita Economos [a,b,*], Patrick Boehnke [b,c], Alain Burgisser [d,e]

[a] *Roy M. Huffington Department of Earth Sciences, Southern Methodist University, P.O. Box 750395, Dallas, TX 75275-0395, United States*
[b] *Department of Earth, Planetary and Space Sciences, University of California, 595 Charles Young Drive E., Los Angeles, CA 90095-1567, United States*
[c] *Department of the Geophysical Sciences, The University of Chicago, 5734 South Ellis Avenue, Chicago, IL 60637, United States*
[d] *CNRS-INSU, ISTerre, Le Bourget du Lac, France*
[e] *Université Savoie Mont Blanc, ISTerre, Le Bourget du Lac, France*

Abstract

The mobility and geochemical behavior of sulfur in magmas is complex due to its multi-phase (solid, immiscible liquid, gaseous, dissolved ions) and multi-valent (from S^{2-} to S^{6+}) nature. Sulfur behavior is closely linked with the evolution of oxygen fugacity ($f\text{O}_2$) in magmas; the record of $f\text{O}_2$ evolution is often enigmatic to extract from rock records, particularly for intrusive systems. We apply a novel method of measuring S isotopic ratios in zoned apatite crystals that we interpret as a record of open-system magmatic processes. We interrogate the S concentration and isotopic variations preserved in multiple apatite crystals from single hand specimens from the Cadiz Valley Batholith, CA via electron microprobe and ion microprobe. Isotopic variations in single apatite crystals ranged from 0 to 3.8‰ δ^{34}S and total variation within a single hand sample was 6.1‰ δ^{34}S. High S concentration cores yielded high isotopic ratios while low S concentration rims yielded low isotopic ratios. We discuss a range of possible natural scenarios and favor an explanation of a combination of magma mixing and open-system, ascent-driven degassing under moderately reduced conditions: $f\text{O}_2$ at or below NNO+1, although the synchronous crystallization of apatite and anhydrite is also a viable scenario. Our conclusions have implications for the coupled S and $f\text{O}_2$ evolution of granitic plutons and suggest that in-situ apatite S isotopic measurements could be a powerful new tool for evaluating redox and S systematics in magmatic systems.
© 2017 Elsevier Ltd. All rights reserved.

1. INTRODUCTION

The behavior of sulfur in magmas is inexorably linked to oxygen fugacity ($f\text{O}_2$) due to the wide valence state variability of S, from S^{2-} to S^{6+}. Sulfur in magmas can exist as solid sulfate or sulfide phases, immiscible sulfide liquids, as ions in solution, or as a multi-phase gas and can therefore have complex evolution in magmatic rocks. Thus, the evolution of S phases during magmatic processes is challenging to constrain in natural systems. This is particularly true in ancient systems where the gas component is lost. Furthermore, for the intrusive parts of magmatic systems, complex mixing behaviors obscure the relative chronological constraints typically provided by melt inclusion-matrix glass comparisons applied to mafic extrusive rocks

---

* Corresponding author at: Roy M. Huffington Department of Earth Sciences, Southern Methodist University, P.O. Box 750395, Dallas, TX 75275, United States.
E-mail addresses: reconomos@smu.edu (R. Economos), pboehnke@gmail.com (P. Boehnke), alain.burgisser@univ-savoie.fr (A. Burgisser).

(Wallace and Edmonds, 2011; Cottrell and Kelley, 2011; Moussallam et al., 2014). The bulk ratio of plutonic to volcanic materials in continental arcs, for example, is up to 10:1 (White et al., 2006), indicating that the crustal-scale S phase distribution and related magma fO_2 evolution are dominated by intrusive processes.

Dissolved S in magmas exists primarily in two valence states, sulfide (S^{2-}) and sulfate (S^{6+}), although intermediate valence ions may also be present (Métrich et al., 2009; Konecke et al., 2017). The transition from sulfide to sulfate (or vice-versa) as the dominant magmatic S species occurs over the range of fO_2 typically observed in terrestrial magmas, from approximately nickel-nickel oxide buffer values of NNO+1 to NNO+3 (this corresponds to the quartz-fayalite-magnetite buffer [QFM] to QFM+2), suggesting that many magmas likely contain multi-valent S speciation (Carroll and Rutherford, 1988; Jugo et al., 2005, 2010; Klimm et al., 2012). In addition to its sensitivity to fO_2 changes, S also exhibits a strong isotopic fractionation as a consequence of bonding environments in different valence states of S^{2-} and S^{6+} that can be several per mil (‰) at magmatic temperatures, with S^{2-} relatively enriched in ^{32}S and S^{6+} relatively enriched in ^{34}S (Harrison and Thode, 1957; Sakai, 1968). The utility of direct measurement of this isotopic fractionation in volcanic glasses and melt inclusions is currently being explored via laboratory experiments and in natural sample suites (Mandeville et al., 2009; Moussallam et al., 2014; Fiege et al., 2014). Alternatively, in a scenario in which multiple valence states are present in a magma, an isotopic fractionation associated with each species will be inherited by crystallizing minerals that incorporate S as a major element (such as sulfide and sulfate minerals) or as a trace element. Efforts are underway to combine these records in volcanic systems (Beaudry et al., 2015). However, as noted, the non-linear, sometimes cyclical nature of the evolution of intrusive igneous systems (Miller et al., 2007; Cooper and Kent, 2014; Barboni et al., 2016) that crystallize to the solidus makes interpreting melt inclusion data challenging.

Apatite is recognized as a zoned carrier of S (Streck and Dilles, 1998; Tepper and Kuehner, 1999; Parat et al., 2002; Chambefort et al., 2008; Van Hoose et al., 2013; Stock et al., 2015) (Fig. 1), but calculating magma S concentrations from apatite S concentrations is hampered by several complications. Sulfate has a much higher partition coefficient in apatite then sulfide, causing the bulk partition coefficient of S into apatite to be highly fO_2 dependent, in addition to dependencies on temperature (Peng et al., 1997; Parat and Holtz, 2005). This effect is layered on variability of the solubility of the multiple S species at changing pressure, temperature, compositional and fO_2 environments (Carroll and Rutherford, 1988; Wallace and Carmichael, 1992; Ducea et al., 1994, 1999; Clemente et al., 2004; Liu et al., 2007; Jugo, 2009; Baker and Moretti, 2011; Klimm et al., 2012).

In contrast, this study capitalizes on the partitioning of S into apatite as a high concentration trace element (0.1–1 wt.% SO_3) (Ohmoto, 1986; Peng et al., 1997; Parat and Holtz, 2005), to make the first measurements of ^{32}S and ^{34}S isotopes at high precision in situ via secondary ion mass
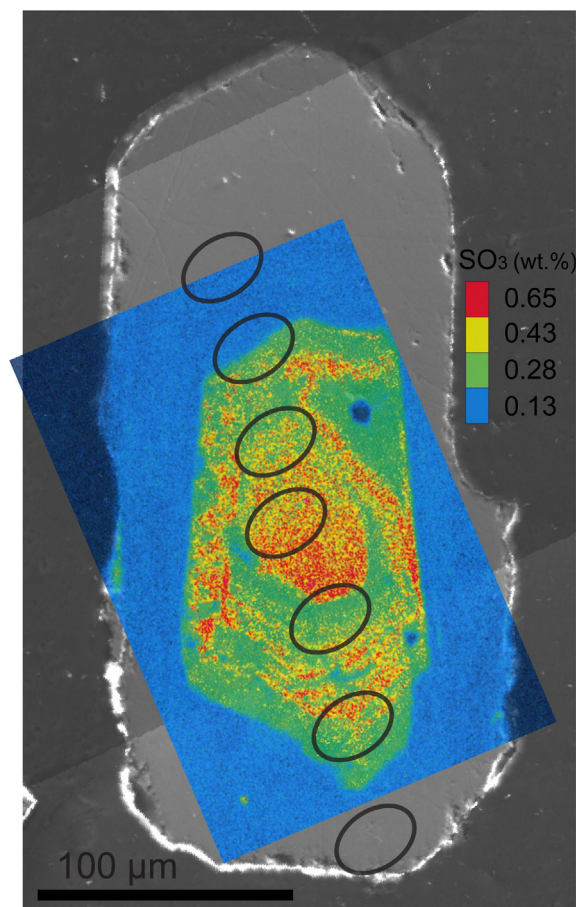

Fig. 1. *Sulfur elemental zoning and SIMS analytical spots in a representative apatite crystal.* Example of sub-micron scale sulfur concentration (measured via EPMA) zoning preserved in an apatite crystal 756-35, with high sulfur concentration core and a low sulfur concentration rim. Oscillatory zoning is followed by a steep drop in concentration to a homogeneously low concentration that represents the dominant zoning pattern of surveyed grains. Areas of subsequent ion microprobe spots are overlain.

spectrometry (SIMS) (Fig. 1). Exploration of S concentration in concert with isotopic ratios yields unique information about the S behavior variations and the processes that drive them. This record has the added advantage of good preservation in plutonic rocks, such as the ones utilized in this study, and constraints provided by the relative chronology of crystal zoning.

Samples for this study are from the Cadiz Valley Batholith, a Cretaceous upper crustal California-type batholith (Howard, 2002; Barth et al., 2004). This batholith is representative of a family of intrusive suites, the observation of which has been integral to modern understanding of magmatic processes (Bateman and Chappell, 1979; Kistler et al., 1986; Coleman and Glazner, 1997; Paterson et al., 2011). These magmas were of the 'cool, wet' affinity (Deering et al., 2010) thus their generally low temperatures provide the highest likelihood of preserving mineral zoning that was minimally disturbed by diffusion. Indeed, fine-scale S zoning with sharp boundaries as shown by Streck

and Dilles (1998) and found in this study suggest that that S substitution in apatite is highly resistant to diffusion (Fig. 1).

The mineral apatite is stable over a wide magma compositional range (Harrison and Watson, 1984; Piccoli and Candela, 2002) and is found in abundance information environments as diverse as lunar basalts and Yellowstone rhyolites (Boyce et al., 2010; Bindeman and Valley, 2001). The type of record documented here should be present in any system that is sufficiently oxidized to contain sulfate and that crystallizes apatite.

2. SAMPLES

An axis of voluminous Cretaceous Cordilleran batholiths stretches across western North America, representing a canonical case of intrusive magmatic suites (Coleman and Glazner, 1997). Samples for this study are from the Cadiz Valley Batholith, located in the central Mojave Desert of Southern California. This batholith is Late Cretaceous (Barth et al., 2004) and was intruded at a pressure of ~150 MPa, estimated from Al-in-hornblende barometry (Anderson, 1998). Evidence that a volcanic edifice overlaid this system is preserved in detrital materials in regional Cretaceous sedimentary basins (Barth et al., 2013). The batholith is composed of muscovite-bearing granites to hornblende granodiorites (Howard, 2002).

Apatites for this study were extracted from one granite and one granodiorite sample. Sample 756, which yielded six of the seven analyzed apatite grains, is a coarsegrained granite sample of approximately eutectic mineralogy. Phases include plagioclase feldspar, K-feldspar, quartz, biotite and muscovite. Apatite, monazite, and zircon are accessory phases in this sample. Opaque phases present include magnetite and ilmenite, determined by energy-dispersive spectrometry conducted with an EDAX detector on the LEO1430 scanning electron microscope at UCLA. Apatites in sample 756 are included throughout the major phase assemblage, within plagioclase, K-feldspar and quartz. Sample 760 is a medium-grained granodiorite containing hornblende and biotite. Titanite, apatite and zircon are accessory phases, in addition to minor allanite. Magnetite was the only opaque phase identified in this sample. Apatites in sample 760 are included in plagioclase and hornblende crystals. The abundance of water-bearing minerals such as biotite and hornblende and prominent zircon inheritance indicate that these magmas had high water contents and cool liquidus temperatures (Moore and Carmichael, 1998; Economos et al., 2011; Miller et al., 2007; Deering et al., 2010). Sample 760 is interpreted to have crystallized from a magma that was closely/genetically related to sample 756 due to the proximity and contiguity of the two plutons from which they originate.

Neither primary S-bearing mineral species such as sulfide or anhydrite were observed microscopically or by Energy Dispersive Spectroscopy via Scanning Electron Microscope in thin sections of either sample. It is possible that sulfides are too small or rare to be observed in thin section. The possible role of sulfide crystallization is therefore addressed in the discussion of apatite geochemistry.

Anhydrite is found in intermediate and felsic igneous rocks in a variety of settings (e.g. Carroll and Rutherford, 1987; Barth and Dorais, 2000; Chambefort et al., 2008). It is possible that anhydrite was present but destroyed during thin section preparation due to its solubility in water. We address this possibility by examining the apatite mineral inclusion population via dry and water-free preparation techniques.

Ten grains from sample 756 were bisected using a Hitachi IM4000 Ar-ion mill in order to create a fresh cut without the use of water to explore the possible presence of highly soluble anhydrite inclusions in apatites. Anhydrite inclusions within apatite might be expected since these minerals are often spatially associated (e.g. Tepper and Kuehner, 1999; Chambefort et al., 2008). A mount not used in the isotope study (M1) was polished with water-based techniques to expose apatite centers. The epoxy block was subsequently loaded with an orientation for a perpendicular cut by the Hitachi IM4000 Ar-ion mill to bisect apatite grains. A mask with micron-scale precision was used to control the location of the milling relative to the sample surface. Approximately 30 μm of material were removed from the sample surface, exposing a number of inclusions that were not previously exposed at the surface. These inclusions were typically completely encased in apatite and did not reside along visible fractures. The mineralogy of these inclusions was characterized using an EDAX energy dispersive detector mounted on a Leo VP1450 scanning electron microscope at Southern Methodist University. Mineral inclusions observed were zircon, feldspar, biotite and quartz, and no anhydrite was identified (Fig. 2). Sections of rock samples were also polished in alcohol and surveyed via energy dispersive spectroscopy. No anhydrite was observed.

3. METHODS

Apatite integrates high concentrations of S up to 2000 ppm or more, dominantly in the sulfate state into its crystal lattice in place of PO_4^{3-} (Parat and Holtz, 2004, 2005; Parat et al., 2011), although recent studies show that subordinate sulfide or sulfite components can be present
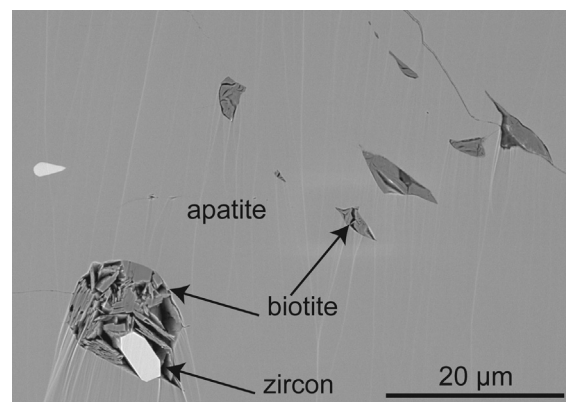

Fig. 2. Biotite and zircon inclusions in an apatite grain prepared using the Hitachi IM4000 Ar-ion mill.

(Konecke et al., 2017). The dominance of sulfate in studied apatites was confirmed via electron microprobe measurements (see Electronic Annex [E.A.]). These high S concentrations and the high electronegativity (and thus ionization potential) of S allow us to measure high precision $\delta^{34}S_{(CDT)}$ ratios in situ by SIMS. In some cases, the 1σ precisions achieved are an order of magnitude smaller than the observed range of $\delta^{34}S_{(CDT)}$ resulting from the large isotopic fractionations of multi-valent S.

A matrix-matched standard is required to quantify instrumental mass fractionations between isotopes of the same element in order to calculate isotopic ratios via SIMS. Since there was no existing S isotope standard for apatite, one was characterized for this study. A single apatite crystal from Durango, MX (UCLA-D1, referred to as 'D1' in Table 1) was characterized for elemental and isotopic homogeneity via in situ techniques (see E.A. for additional information). This crystal contains 0.36 ± 0.02 wt.% SO_3. Its absolute isotopic ratio was determined via gas source mass spectrometry at the University of California, San Diego via methods described by Farquhar et al. (2002). Sulfur isotopic compositions are reported in $\delta^{34}S_{CDT} = [((^{34}S/^{32}S)_{sample} - (^{34}S/^{32}S)_{CDT})/(^{34}S/^{32}S)_{CDT}] \times 1000$, where CDT refers to the Canyon Diablo Troilite S isotope standard (Beaudoin et al., 1994; see Ding et al., 2001 for conversion relative to Vienna-CDT). Three analyses of the UCLA-D1 apatite measured via gas source mass spectrometry relative to CDT yielded consistent results of $\delta^{34}S_{(CDT)}$ values of $0.34 \pm 0.022‰$ (1σ stdev) and $\Delta^{33}S_{(CDT)}$ values of $-0.069 \pm 0.02‰$ (1σ stdev) (E.A.).

Hundreds of apatite crystals from samples 756 and 760 were separated from 50 to 400 μm size fractions via heavy liquids and mounted parallel to c-axes on three one-inch round epoxy mounts and polished with 1200 grit and 3 and 1 μm diamond polish to expose grain cores without damaging crystals. Typical apatite dimensions were 100×250 μm, allowing for detailed S concentration mapping via electron microprobe. Mounts were coated with carbon and analyzed using the JEOL SuperProbe electron microprobe at University of California, Los Angeles. Sulfur and a suite of other elements were analyzed using a 30 nA beam with an accelerating voltage of 15 KeV. Sulfur was analyzed on a PET spectrometer with 60 s peak count times and 15 s background count times, yielding ∼100–300 counts per second for a range of low to high S concentration grains. Barite was used as a sulfate standard for peak identification. Migration of S during analysis was not expected as analyses were conducted perpendicular to c-axes and no variation in S X-ray intensity was observed during individual analyses (Pyle et al., 2002). Grains were surveyed with line transects of four to five points from cores to rims with an abbreviated element list designed for rapid survey. Representative full analyses indicated that these grains are of the fluorapatite end member (E.A.) and F and Cl were excluded from subsequent analyses to improve efficiency. Any grains yielding anomalously high S concentrations were explored in more detail with mapping of S concentrations. Sulfur concentration maps were collected with pixel sizes ranging from 0.5 to 3 μm depending on the apparent complexity of the zoning in the target grain.

Sulfur was collected for 0.5 s per pixel with a beam current of 30 nA.

Sulfur isotopic data were collected on the CAMECA IMS1270 at the University of California, Los Angeles in multi-collection mode. A 6–7 nA, 15–20 μm diameter Cs^+ primary beam was used. An electron flood gun was used to compensate for charge build-up from primary beam impact. Mass resolution was set at ∼5000 mass resolving power to separate ^{32}S from O_2 and PH mass peaks. The number of 10-s cycles taken for each spot varied based on the total counts – higher count rate spots were counted for fewer cycles. The number of cycles (from 20 to 40) was selected based on the desired analytical uncertainty. The isotopic ratio was monitored during the analysis to ensure that no statistically significant *within-analysis* drift occurred, allowing for the comparison of spots with varying numbers of cycles.

Typical ^{32}S CPS were 2 to 5×10^6 and were therefore measured via Faraday cup. Meanwhile, ^{34}S CPS under these conditions were 1 to 4×10^5 and were measured using an electron multiplier. The errors associated with the background correction on the Faraday cup (determined at the beginning of each analysis) and the dead time correction on the electron multiplier (deadtime of 28 s determined prior to analysis) were minimized by varying the primary beam intensity to achieve optimum reproducibility. A single primary beam setting was used for blocks of analyses, with all unknowns bracketed by standard analyses.

Reproducibility of standard analyses and errors associated with the internal reproducibility of each analytical point were considered when calculating reported errors for each SIMS measurement. The standard deviation of values for UCLA-D1 analyses for all standards was used for the 'external' reproducibility. Standard error for each analytical point was used for the 'internal' reproducibility. These two values were added in quadrature to arrive at an individual error for each datum. For analyses with high count rates, the error is dominated by the external reproducibility. For analyses with low count rates, the internal error contributes a larger fraction to the overall uncertainty of the datum.

Due to the sub-micron scale S concentration zoning in many of the apatite cores, there is a high likelihood that the SIMS spot averaged across some heterogeneous sampling of these zones. Direct calculation of S concentrations from SIMS analysis was not possible due to the inability to measure a stoichiometric element for normalization in static (multicollection) mode. A strategy was therefore developed to estimate the S concentration for the footprint of the ion microprobe spot. After SIMS analyses, geometry of ion probe pits was explored through secondary electron detection using a scanning electron microscope. As a köhler illumination was utilized, areas of flat pit bottoms were assumed to represent the best estimate of the footprint of collected ions. The area of this footprint was mapped onto pre-SIMS analysis S zoning maps. Additional electron probe spot analyses were conducted in areas around the grain that captured the total range of variation of S concentrations in the grain. The areas of these electron microprobe spots were clearly observable in backscattered electron

Table 1
SIMS sulfur isotopic data.

	^{32}S CPS	^{32}S 1σ err	^{34}S CPS	^{34}S 1σ err	^{34}S/^{32}S	^{34}S/^{32}S 1σ err	Uncorrected δ^{34}S ‰	1σ err	Corrected δ^{34}S ‰	1σ err	S conc. wt.% SO$_3$	1σ err
Mount 2												
D1@1	7.88E+06	2.42E+05	3.48E+05	1.07E+04	0.044136	8.55E−06	−0.60	0.19	0.66	0.38		
D1@2	7.97E+06	2.42E+05	3.52E+05	1.07E+04	0.044132	6.85E−06	−0.68	0.16	0.62	0.36		
D1@3	8.02E+06	2.44E+05	3.54E+05	1.08E+04	0.044129	6.49E−06	−0.76	0.15	0.59	0.35		
D1@4	8.15E+06	2.40E+05	3.59E+05	1.06E+04	0.044109	6.63E−06	−1.21	0.15	0.17	0.35		
760-50@0	3.93E+06	3.22E+03	1.75E+05	1.38E+02	0.044434	8.96E−06	6.15	0.20	7.15	0.38		
760-50@1	3.58E+06	2.16E+03	1.59E+05	1.06E+02	0.044435	9.42E−06	6.17	0.21	7.14	0.39		
760-50@2	3.61E+06	2.88E+03	1.60E+05	1.32E+02	0.044452	8.98E−06	6.56	0.20	7.48	0.38	0.18	0.053
76050@3	5.03E+06	4.14E+03	2.24E+05	1.83E+02	0.044498	8.83E−06	7.60	0.20	8.48	0.38	0.27	0.053
760-50@4	5.04E+06	4.72E+03	2.24E+05	2.17E+02	0.044476	6.22E−06	7.10	0.14	7.93	0.35	0.26	0.053
760-50@5	6.26E+06	1.64E+04	2.79E+05	7.23E+02	0.044509	7.47E−06	7.84	0.17	8.63	0.36	0.29	0.053
760-50@6	6.44E+06	1.47E+04	2.87E+05	6.42E+02	0.044499	8.17E−06	7.63	0.19	8.38	0.37	0.34	0.053
760-50@7	5.80E+06	1.99E+04	2.58E+05	8.82E+02	0.044483	7.72E−06	7.25	0.17	7.96	0.37	0.32	0.053
760-50@8	6.26E+06	1.99E+04	2.78E+05	8.89E+02	0.044497	6.98E−06	7.56	0.16	8.23	0.36	0.35	0.053
760-50@9	4.55E+06	1.44E+04	2.02E+05	6.40E+02	0.044463	7.22E−06	6.80	0.16	7.42	0.36	0.34	0.053
760-50@10	4.03E+06	4.98E+03	1.79E+05	2.37E+02	0.044415	9.18E−06	5.72	0.21	6.30	0.38	0.18	0.053
760-50@11	4.04E+06	2.93E+03	1.79E+05	1.23E+02	0.044397	7.82E−06	5.32	0.18	5.85	0.37	0.19	0.053
D1@5	8.11E+06	2.50E+05	3.58E+05	1.10E+04	0.044096	7.04E−06	−1.51	0.16	0.43	0.36		
D1@6	7.93E+06	2.52E+05	3.50E+05	1.11E+04	0.044087	8.86E−06	−1.72	0.20	0.26	0.38		
D1@7	8.17E+06	2.50E+05	3.60E+05	1.10E+04	0.044079	7.78E−06	−1.90	0.18	0.12	0.37		
D1@8	8.30E+06	2.51E+05	3.66E+05	1.11E+04	0.044081	6.73E−06	−1.85	0.15	0.22	0.36		
756-35@0	3.54E+06	2.63E+03	1.57E+05	1.21E+02	0.044262	1.02E−05	2.26	0.23	2.58	0.40	0.14	0.018
756-35@1	1.05E+07	1.55E+04	4.67E+05	6.82E+02	0.044341	4.77E−06	4.03	0.11	4.31	0.34	0.53	0.018
756-35@2	1.50E+07	1.90E+04	6.67E+05	8.34E+02	0.044345	6.96E−06	4.13	0.16	4.37	0.36	0.52	0.018
756-35@3	1.54E+07	1.38E+04	6.81E+05	5.47E+02	0.044355	6.44E−06	4.35	0.15	4.55	0.35	0.63	0.018
756-35@4	1.14E+07	1.43E+04	5.04E+05	6.39E+02	0.044324	4.98E−06	3.65	0.11	3.81	0.34	0.55	0.018
756-35@5	3.43E+06	4.06E+03	1.51E+05	1.85E+02	0.044181	9.79E−06	0.42	0.22	0.54	0.39	0.29	0.018
756-35@6	2.94E+06	3.32E+03	1.30E+05	1.42E+02	0.044205	1.15E−05	0.96	0.26	1.03	0.41	0.13	0.018
D1@9	8.16E+06	2.44E+05	3.59E+05	1.08E+04	0.044067	7.84E−06	−2.17	0.18	0.28	0.37		
D1@10	7.99E+06	2.50E+05	3.52E+05	1.10E+04	0.044055	7.52E−06	−2.44	0.17	0.05	0.36		
D1@11	6.85E+06	2.09E+05	3.02E+05	9.27E+03	0.044038	1.18E−05	−2.83	0.27	−0.30	0.42		
D1@13	6.17E+06	1.92E+05	2.72E+05	8.48E+03	0.044035	1.59E−05	−2.88	0.36	−0.26	0.48		
D1@14	6.34E+06	1.85E+05	2.79E+05	8.15E+03	0.044058	1.16E−05	−2.36	0.26	0.30	0.41		
D1@15	7.20E+06	2.43E+05	3.17E+05	1.07E+04	0.044063	1.21E−05	−2.26	0.27	0.44	0.42		
Mount 3												
D1@3	1.00E+07	2.69E+03	4.41E+05	1.12E+02	0.043992	5.92E−06	−3.87	0.13	0.49	0.29		
D1@4	9.71E+06	5.11E+03	4.27E+05	2.18E+02	0.043993	8.42E−06	−3.85	0.19	0.51	0.32		
D1@5	1.02E+07	3.49E+03	4.49E+05	1.42E+02	0.044000	4.50E−06	−3.68	0.10	0.68	0.28		
D1@6	1.00E+07	2.80E+03	4.40E+05	1.42E+02	0.043995	6.62E−06	−3.79	0.15	0.57	0.30		
D1@7	9.95E+06	4.77E+03	4.38E+05	2.13E+02	0.043984	4.82E−06	−4.03	0.11	0.32	0.28		
756-18@0	3.39E+06	2.19E+03	1.50E+05	9.82E+01	0.044258	1.09E−05	2.15	0.25	6.51	0.36		
756-18@1	3.98E+06	2.21E+03	1.76E+05	1.04E+02	0.044255	1.23E−05	2.08	0.28	6.44	0.38		

Table 1 (*continued*)

	^{32}S CPS	^{32}S 1σ err	^{34}S CPS	^{34}S 1σ err	$^{34}S/^{32}S$	$^{34}S/^{32}S$ 1σ err	Uncorrected $\delta^{34}S$ ‰	1σ err	Corrected $\delta^{34}S$ ‰	1σ err	S conc. wt.% SO_3	1σ err
756-18@2	3.99E+06	2.31E+03	1.76E+05	8.71E+01	0.044197	1.13E−05	0.78	0.26	5.14	0.37		
756-18@3	4.69E+06	1.28E+03	2.08E+05	6.74E+01	0.044216	9.68E−06	1.21	0.22	5.57	0.34	0.19	0.019
756-18@5	9.07E+06	5.24E+04	4.01E+05	2.32E+03	0.044276	8.64E−06	2.56	0.20	6.92	0.33	0.31	0.019
756-18@6	5.46E+06	5.57E+03	2.42E+05	2.42E+02	0.044231	7.35E−06	1.55	0.17	5.91	0.31	0.23	0.019
756-18@7	4.20E+06	4.27E+03	1.86E+05	1.77E+02	0.044208	9.34E−06	1.03	0.21	5.38	0.34	0.19	0.019
D1@8	9.62E+06	3.97E+03	4.23E+05	1.85E+02	0.043970	6.50E−06	−4.36	0.15	0.00	0.30		
D1@9	9.50E+06	4.42E+03	4.18E+05	2.02E+02	0.043973	6.28E−06	−4.30	0.14	0.06	0.30		
D1@10	9.58E+06	1.06E+04	4.21E+05	4.56E+02	0.043974	7.88E−06	−4.27	0.18	0.09	0.32		
D1@13	8.43E+06	5.27E+03	3.72E+05	2.45E+02	0.044097	5.35E−06	−1.49	0.12	0.90	0.43		
D1@14	8.58E+06	3.62E+03	3.78E+05	1.75E+02	0.044097	6.61E−06	−1.50	0.15	0.90	0.44		
D1@15	8.34E+06	3.85E+03	3.68E+05	1.73E+02	0.044083	7.04E−06	−1.80	0.16	0.59	0.45		
D1@16	8.71E+06	4.49E+03	3.84E+05	1.90E+02	0.044073	6.73E−06	−2.03	0.15	0.37	0.44		
D1@17	8.35E+06	3.43E+03	3.68E+05	1.63E+02	0.044075	6.29E−06	−1.97	0.14	0.42	0.44		
D1@18	8.40E+06	5.79E+03	3.70E+05	2.48E+02	0.044048	7.23E−06	−2.60	0.16	−0.20	0.45		
D1@19	8.98E+06	3.45E+03	3.96E+05	1.60E+02	0.044070	5.89E−06	−2.10	0.13	0.29	0.44		
D1@20	8.44E+06	3.50E+03	3.72E+05	1.62E+02	0.044038	6.53E−06	−2.81	0.15	−0.42	0.44		
D1@21	9.13E+06	4.34E+03	4.03E+05	1.98E+02	0.044092	5.29E−06	−1.60	0.12	0.80	0.43		
D1@22	8.86E+06	4.75E+03	3.91E+05	2.25E+02	0.044066	6.53E−06	−2.18	0.15	0.21	0.44		
D1@23	9.10E+06	5.35E+03	4.01E+05	2.33E+02	0.044082	6.71E−06	−1.82	0.15	0.57	0.44		
756-37@0	3.61E+06	1.59E+03	1.60E+05	6.99E+01	0.044301	9.08E−06	3.13	0.21	5.52	0.46		
756-37@1	3.98E+06	1.82E+03	1.76E+05	8.06E+01	0.044310	8.71E−06	3.33	0.20	5.73	0.46	0.18	0.016
756-37@2	3.38E+06	1.42E+03	1.50E+05	6.38E+01	0.044352	8.31E−06	4.29	0.19	6.68	0.46	0.16	0.016
756-37@3	8.38E+06	3.85E+03	3.71E+05	1.16E+02	0.044341	1.57E−05	4.03	0.36	6.43	0.55	0.26	0.016
756-37@4	7.25E+06	7.81E+03	3.21E+05	4.22E+02	0.044320	1.37E−05	3.56	0.31	5.96	0.52	0.26	0.016
D1@25	9.17E+06	3.28E+03	4.04E+05	1.64E+02	0.044056	6.08E−06	−2.40	0.14	−0.01	0.44		
D1@26	9.40E+06	3.53E+03	4.14E+05	1.51E+02	0.044057	6.66E−06	−2.38	0.15	0.01	0.44		
Mount 4												
D1@13	7.34E+06	7.20E+03	3.23E+05	3.29E+02	0.044026	7.92E−06	−3.09	0.18	0.20	0.34		
D1@14	5.80E+06	2.89E+03	2.55E+05	1.33E+02	0.044003	8.53E−06	−3.62	0.19	−0.29	0.35		
D1@15	5.71E+06	2.42E+03	2.52E+05	1.02E+02	0.044029	7.01E−06	−3.03	0.16	0.36	0.33		
D1@16	5.62E+06	4.09E+03	2.47E+05	1.87E++02	0.044023	5.45E−06	−3.17	0.12	0.26	0.31		
D1@17	5.68E+06	4.81E+03	2.50E+05	2.11E+02	0.044023	6.55E−06	−3.17	0.15	0.31	0.32		
D1@18	5.60E+06	3.30E+03	2.46E+05	1.43E+02	0.044021	7.70E−06	−3.21	0.17	0.31	0.34		
756-95@0	2.54E+06	1.50E+03	1.13E+05	1.04E+02	0.044310	2.08E−05	3.34	0.47	4.64	0.55	0.14	0.015
756-95@1	3.88E+06	5.40E+03	1.72E+05	2.38E+02	0.044290	1.34E−05	2.89	0.30	4.15	0.42	0.26	0.015
756-95@2	6.11E+06	2.64E+04	2.71E+05	1.18E+03	0.044371	5.88E−06	4.73	0.13	5.93	0.32	0.42	0.015
756-95@3	8.07E+06	1.19E+04	3.58E+05	5.28E+02	0.044361	4.37E−06	4.50	0.10	5.66	0.30	0.46	0.015
756-95@4	7.91E+06	6.12E+03	3.51E+05	2.60E+02	0.044358	6.68E−06	4.43	0.15	5.55	0.32	0.47	0.015
756-95@5	2.53E+06	9.86E+02	1.12E+05	4.30E+01	0.044333	9.35E−06	3.86	0.21	4.94	0.36	0.15	0.015
D1@19	5.74E+06	3.50E+03	2.53E+05	1.50E+02	0.044031	7.24E−06	−2.99	0.16	0.85	0.33		
D1@20	5.73E+06	2.48E+03	2.52E+05	1.06E+02	0.044024	6.34E−06	−3.13	0.14	0.75	0.32		
D1@21	5.72E+06	8.86E+03	2.52E+05	3.82E+02	0.044008	7.18E−06	−3.50	0.16	0.42	0.33		

	^{32}S CPS	^{32}S SE	^{34}S CPS	^{34}S SE	raw ^{32}S/^{34}S	SE	raw δ^{34}S$_{(CDT)}$	SE	calc δ^{34}S$_{(CDT)}$	error	SO$_3$ wt.%	error
D1@22	5.73E+06	3.57E+03	2.52E+05	1.59E+02	0.044016	6.83E−06	−3.32	0.15	0.65	0.33		
756-38@0	2.00E+06	2.32E+03	8.88E+04	1.04E+02	0.044343	1.21E−05	4.09	0.27	4.94	0.40	0.15	0.017
756-38@1	3.88E+06	3.12E+03	1.72E+05	1.29E+02	0.044293	1.02E−05	2.95	0.23	3.75	0.37	0.26	0.017
756-38@2	9.14E+06	9.07E+03	4.05E+05	3.83E+02	0.044307	5.71E−06	3.27	0.13	4.02	0.31	0.50	0.017
756-38@3	5.78E+06	3.54E+03	2.56E+05	1.57E+02	0.044305	7.61E−06	3.23	0.17	3.94	0.33	0.39	0.017
756-38@4	2.56E+06	1.22E+03	1.13E+05	5.82E+01	0.044294	1.23E−05	2.97	0.28	3.64	0.40	0.18	0.017
D1@23	5.62E+06	4.11E+03	2.47E+05	1.84E+02	0.043992	8.13E−06	−3.86	0.18	0.38	0.34		
D1@24	5.61E+06	2.72E+03	2.47E+05	1.29E+02	0.043999	7.06E−06	−3.70	0.16	0.58	0.33		
D1@25	5.65E+06	4.47E+03	2.49E+05	2.14E+02	0.043996	8.47E−06	−3.78	0.19	0.55	0.34		
D1@26	5.60E+06	3.72E+03	2.46E+05	1.76E+02	0.043965	7.51E−06	−4.48	0.17	−0.10	0.33		
D1@27	5.76E+06	4.14E+03	2.53E+05	1.87E+02	0.043987	5.56E−06	−3.97	0.13	0.46	0.31		
756-76@6	2.22E+06	1.26E+03	9.82E+04	6.20E+01	0.044239	1.23E−05	1.72	0.28	2.12	0.40	0.13	0.018
756-76@7	2.38E+06	1.70E+03	1.05E+05	7.71E+01	0.044229	1.18E−05	1.51	0.27	1.86	0.39	0.16	0.018
756-76@8	4.86E+06	7.07E+03	2.15E+05	3.31E+02	0.044253	8.60E−06	2.04	0.19	2.34	0.35	0.35	0.018
756-76@9	4.66E+06	1.24E+04	2.06E+05	5.54E+02	0.044275	7.77E−06	2.54	0.18	2.80	0.34	0.32	0.018
756-76@10	6.12E+06	4.25E+03	2.71E+05	2.23E+02	0.044262	1.08E−05	2.25	0.24	2.46	0.38	0.45	0.018
756-76@11	4.98E+06	3.11E+03	2.20E+05	1.43E+02	0.044280	7.60E−06	2.65	0.17	2.82	0.33	0.33	0.018
D1@28	5.67E+06	3.27E+03	2.49E+05	1.35E+02	0.043969	8.35E−06	−4.38	0.19	0.36	0.34		
D1@29	5.69E+06	2.15E+03	2.50E+05	1.02E+02	0.043949	8.03E−06	−4.84	0.18	−0.05	0.34		
D1@30	6.45E+06	3.29E+03	2.83E+05	1.41E+02	0.043954	5.67E−06	−4.73	0.13	0.11	0.31		
D1@31	6.44E+06	5.33E+03	2.83E+05	2.33E+02	0.043963	6.31E−06	−4.51	0.14	0.36	0.32		

Raw counts per second (CPS) of ^{32}S and ^{34}S and associated standard error, raw ^{32}S/^{34}S and associated standard error, raw δ^{34}S$_{(CDT)}$ and associated standard error, calculated δ^{34}S$_{(CDT)}$ after linear drift and instrumental mass fractionation corrections and associated error, SO$_3$ concentration in wt.% and associated error. See E.A. for detailed descriptions of corrections and text for concentration calculation methods.

detection after analysis. These areas were also mapped onto the original grayscale S variation images. A linear correlation between average grayscale values for electron microprobe spots and measured electron microprobe concentrations was determined for each grain. Excellent linear fits were achieved for each grain, with R^2 values above 0.9, except for grain 760-50 which yielded a value of 0.83. Average grayscale values for SIMS pit areas were then calculated and linear correlations were used obtain concentrations at the same locations as those measured with the SIMS. Uncertainties on concentration variations represent a combination of the uncertainty on the electron microprobe spots and the standard error of the regression of grayscale correlation. Final calculated 1σ uncertainties ranged from 9 to 13%, except grain 760-50, which yielded an uncertainty of 29%. Only isotope measurements that could be correlated with a concentration measurement are plotted in concentration vs. isotopic ratio. Excluded spots include those that fell completely off of electron microprobe concentration maps, marked with concentrations of N/A in Table 1. For spots partially overlapping concentration-mapped areas, the concentration of the overlapping area was used to represent the concentration of the spot.

4. RESULTS

Our electron microprobe survey revealed that apatites typically contain concentrations of ~0.2 wt.% SO_3, while some contain cores with concentrations up to 0.65 wt.% SO_3. These grains demonstrate a drop in wt.% P_2O_5 of a correlative magnitude (see E.A.). Approximately 10% of apatite crystals contain high S cores that were subsequently surveyed in detail using S concentration mapping with pixel sizes ranging from 0.5 to 3 µm (Fig. 3A).

Data from individual grains are described in order of lowest rim isotopic ratio to highest rim isotopic ratio (Fig. 3). Grain 756-35 contains a large core with SO_3 concentrations of 0.52–0.63 wt.%. Complex oscillatory zoning within this core mimics the crystal habit of the core. There is a sharp drop between this core and a monotonically lower S concentration rim that contains ~0.14 wt.% SO_3. Isotopic ratios in the crystal core range from 3.8 to 4.6‰ $\delta^{34}S_{(CDT)}$. Spot 5 in this grain partially intersects the core and rim and yields an anomalously low isotopic ratio of 0.5‰ $\delta^{34}S_{(CDT)}$. This spot is the most significant outlier of the study and lacks a ready explanation. Two spots on the rims of this crystal yield 1.0 and 2.6‰ $\delta^{34}S_{(CDT)}$, which are lower than the core but demonstrate significant diversity within the low S concentration rim. The total $\delta^{34}S$ variation observed in this crystal is 3.6‰, and comparison of the average core and average rim indicates that the S isotopic ratio of the core is 2‰ heavier than that of the rim.

Grain 756-76 contains a core with rough outlines of euhedral crystal faces, but with a mottled internal appearance. This core has a range of concentrations from 0.32 to 0.45 wt.% SO_3. Rim spots have a concentration of ~0.14 wt.% SO_3. An average of 4 spots within this core yields 2.6‰ $\delta^{34}S_{(CDT)}$ and an average of two rim spots yields 2.0‰ $\delta^{34}S_{(CDT)}$. This variation is only slightly outside of analytical error but likely represents a real core-rim variation.

Grain 756-38 contains a complexly shaped core. It shows some suggestion of crystal faces but they appear resorbed and embayed. The core also has a mottled distribution of S. Core spots yield S concentrations between 0.39 and 0.5 wt.% SO_3. A spot overlapping the boundary between core and rim yields a concentration of 0.26 wt.% SO_3 and two spots within the rim yield concentrations of ~0.16 wt.% SO_3. This grain shows no appreciable isotopic variation between core and rim – all are within error of 3.8‰ $\delta^{34}S_{(CDT)}$ excepting a rim spot yielding a ratio of 4.9‰ $\delta^{34}S_{(CDT)}$.

Grain 756-95 contains two euhedral high S concentration zones. One is a sector-zoned crystal and the other is a long, thin crystal. These two cores are aligned along their c-axes. Both have sharp margins. Two spots in the sector-zoned core and one that overlaps with the thin crystal have 0.45 wt.% SO_3. One spot that slightly overlaps the thin crystal contains 0.26 wt.%. SO_3 (although it groups isotopically with rims). The rim of this grain contains 0.15 wt.% SO_3. Three core spots yield an average isotopic ratio of 5.7‰ $\delta^{34}S_{(CDT)}$. Rim spots average 4.5‰ $\delta^{34}S_{(CDT)}$. We interpret that the $\delta^{34}S$ of the core of this crystal is ~1.2‰ higher than the rim.

Grain 756-18 contains a small, angular core with a sharp boundary containing 0.31 wt.% SO_3. This core is surrounded by subtle oscillatory zoning of S that mimics the shape of the moderate S concentration core. Rims of this crystal contain 0.19 wt.% SO_3. One SIMS spot dominantly samples the core, yielding an isotopic ratio of 6.9‰ $\delta^{34}S_{(CDT)}$. One spot mostly samples rim material but slightly overlaps the core, yielding a ratio of 5.9‰ $\delta^{34}S_{(CDT)}$. Two spots that appear to avoid oscillatory zones in the rim yield ratios of 5.4 and 5.6‰ $\delta^{34}S_{(CDT)}$. We interpret that the $\delta^{34}S$ of the core of this crystal is ~1‰ higher than the rim.

Grain 756-37 contains oscillatory S concentration zoning that extends throughout the crystal. This grain also has the lowest range of S concentration from core to rim, from 0.16 to 0.26 wt.% SO_3. Low concentration variation presents a challenge in producing a robust linear correlation to categorize data by the core-rim scheme applicable to other grains. The total isotopic range captured in this crystal is from 5.7 to 6.7‰ $\delta^{34}S_{(CDT)}$.

Grain 760-50 is the only grain analyzed from sample 760. It contains a large core with S concentrations of ~0.3 wt.% SO_3, which are moderately higher than rim concentrations of 0.18 wt.% SO_3. This core has a somewhat mottled appearance. Isotopic ratios in this core range from 7.9 to 8.5‰ $\delta^{34}S_{(CDT)}$, with an average of 8.3‰ $\delta^{34}S_{(CDT)}$. Two spots that intersect the boundary between core and rim yield ratios of 7.4 and 7.5‰ $\delta^{34}S_{(CDT)}$. Rim values are variable, ranging from 5.9 to 7.2‰ $\delta^{34}S_{(CDT)}$, with an average of 6.6‰ $\delta^{34}S_{(CDT)}$. Core spots yield average $\delta^{34}S$ isotopic ratios that are 1.7‰ higher than rim spots.

In summary, the margins of high S cores approximate apatite crystal shapes, with sharp, straight margins suggesting crystal faces. Some cores display fine, concentric oscillatory zoning while others have mottled internal textures. All crystals with high S cores show a sharp drop (<1 µm) between these cores and low S rims. Low S rims yield concentrations between 0.1 and 0.2 wt.% SO_3, which represent
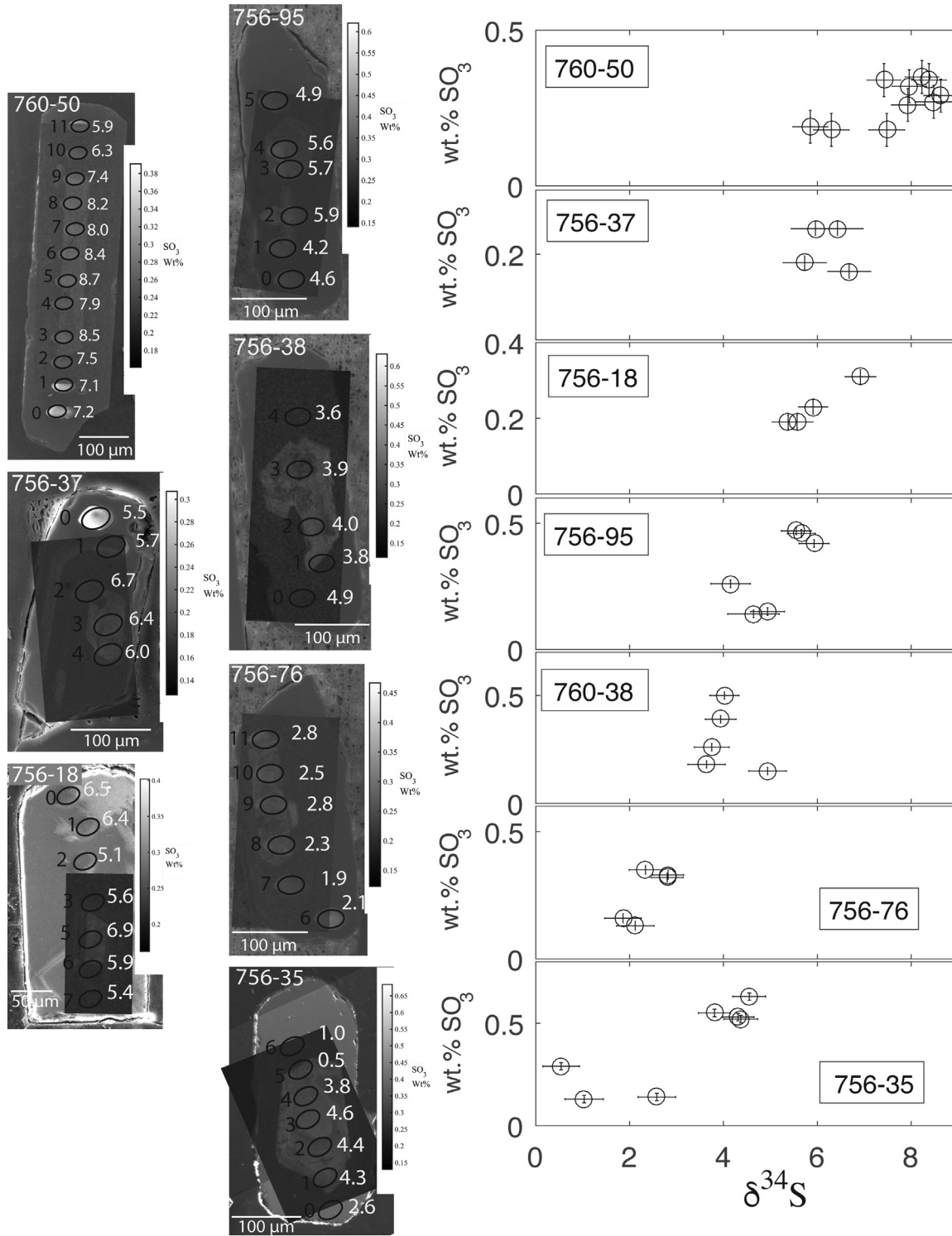
Fig. 3. A. Sulfur concentration zoning (measured via EPMA), SIMS sample locations and $\delta^{34}S_{(CDT)}$ isotopic ratios in all analyzed apatite crystals.

the bulk of overall apatite crystallization as high S cores were only present in ~1/10 surveyed crystals.

Four of the seven analyzed grains show core-rim $\delta^{34}S$ ratio variations of greater than 1‰. The largest core-rim variation observed is 3.8‰ $\delta^{34}S$ (Table 1, Fig. 3). In all

cases in which a statistically significant isotopic variation is observed, $\delta^{34}S$ is higher in high S concentration cores and lower in low S concentration rims.

When low S-concentration rim data is considered alone, an aggregate range of 6.1‰ $\delta^{34}S$ is recorded in apatite rims

of crystals from sample 756, and the total isotopic range including the grain from sample 760 is 8.1‰ δ^{34}S (Fig. 3). This large variation in rim isotopic ratio is accompanied by a very modest decrease in S concentration amongst apatite rims, from ∼0.2 to 0.14 wt.% SO_3.

5. DISCUSSION

5.1. Processes that affect magma S concentration and isotopic ratios

First-order findings of this study include:

1. Significant variations in S isotopic ratios are observed within individual apatite crystals and among apatites from a single hand-sample,
2. These isotopic ratio variations are large considering the high temperatures typical of magmatic systems,
3. Rims of these apatite crystals have equal or lower S isotopic ratios than cores,
4. Where isotopic variations are observed, S concentrations and isotopic ratios are correlated.

Finding #1: Variability in isotopic ratios within and between apatite crystals is observed. Isotopic fractionations are primarily driven when either multi-valent phases are present in a magma, transitions from melt to gas phases occur, or during mixing of magmas with different bulk S isotopic ratios. Numerous workers have explored the fO_2 range at which both sulfate and sulfide are present as dissolved melt phases, which also varies as a function of pressure, Fe content and other physiochemical parameters (Carroll and Rutherford, 1988; Wallace and Carmichael, 1992; Clemente et al., 2004; Jugo et al., 2005; Jugo, 2009; Moretti and Baker, 2008; Klimm et al., 2012), but is typically determined to fall within the range of NNO−1 to NNO+2 for felsic melts at moderate pressures. Variations in fO_2 can directly drive fractionations in the dissolved sulfate and sulfide components of a melt, as depicted in the lever-diagram in Fig. 4. Down-temperature reactions, such as those in Fe-rich systems involving the production of sul-

fate via Fe reduction (e.g. Métrich et al., 2009) will result in similar isotopic behavior. Open system processes, such as magma mixing or S degassing will change the bulk S isotopic ratio (the fulcrum in Fig. 4), thus also changing the ratios of these two components.

Saturation behavior of solid S-bearing phases will exert important controls on magma isotopic variations. Sulfide minerals preferentially partition ^{32}S over ^{34}S, therefore if sulfides crystallize from a melt containing multiple valences of S (depicted only as sulfate and sulfide in Fig. 4), they will remove S with low S isotopic ratio from the melt. The magnitude of this fractionation will be a function of the temperature-dependent S^{6+}-S^{2-} fractionation (e.g. 6.2‰ at 900 °C [Richet et al., 1977, see also Miyoshi et al., 1984 and Li and Liu, 2006]) and also the ratio of sulfate to sulfide in the melt. These variables are represented as the length of and position of the lever in Fig. 4. Thus, in the simplest formulation, sulfide crystallization from a melt that contained both sulfide and sulfate species will drive residual melt S $\delta^{34}S_{(CDT)}$ and therefore sulfate fraction $\delta^{34}S_{(CDT)}$ to higher isotopic ratios. Crystallization of sulfate minerals will have the opposite effect. However, complex combinations of processes such as mineral crystallization and degassing are more realistic for natural magmas and their combined effects have been explored by other workers via modeling (e.g. Marini et al., 1998, 2011).

Open system degassing also drives a range of compositional and isotopic variations based on species that are present in gasses and magmas, which are a function of magma composition, fO_2 and pressure/temperature environment (e.g. Burgisser and Scaillet, 2007). Degassing from highly oxidized melts tends to drive residual melt isotopic ratios toward higher values as dissolved sulfate will preferentially retain ^{34}S relative to all other species. When a mixed speciation is present in the melt, degassing can drive residual isotopic ratios to either higher or lower values depending on the ratio of degassing species (e.g. Sakai, 1968). A significant reversal from positive fractionations to negative fractionations occurs at fO_2 near NNO according to models (Marini et al., 1998, 2011) and NNO+1 according to experimental results (Fiege et al., 2014).

Finding #2: Observed isotopic ratio variations are large. An isotopic variation of greater than 6‰ is recorded in apatites from a single hand sample from a granitic rock in this study. Marini et al. (2011) demonstrate that fractionations of greater than 10‰ can be generated by open-system separation of sulfide minerals. Meanwhile, degassing modeling by Marini et al. (1998, 2011), based on alpha values of Richet et al. (1977), can produce fractionation magnitudes of 8–10‰ for open-system fractionation of a silicate melt at 900 °C containing mixed S valence species. Fractionations are far more modest, in the range of ∼2‰, for closed-system scenarios. Furthermore, Fiege et al. (2014) produced larger than expected fractionations in experimental samples when degassing under conditions more reduced than NNO+1, up to 5‰ in nearly completely degassed samples. The experimental conditions necessitated closed-system degassing, so application of these fractionation factors calculate fractionations of larger magnitudes for open-system cases (see Section 5.3). Thus, closed-system isotopic
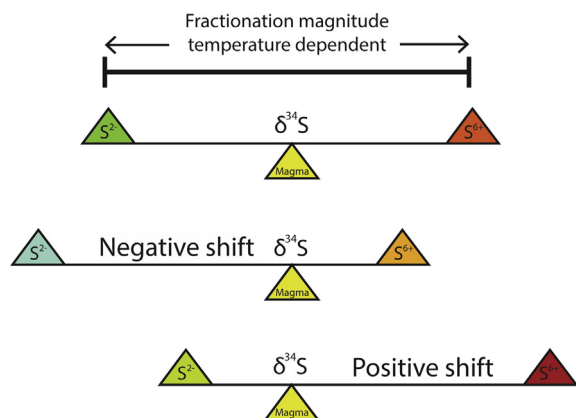

Fig. 4. Schematic diagram highlighting the relationships between $S^{6+}/\Sigma S$ and sulfur isotopic fractionation.

fractionations between sulfate and sulfide at magmatic temperatures are not large enough to explain the observations made in this study. Open system processes must be recorded, either in the form of open-system fractionations of solid phases, open-system degassing, or mixing between magmas with large differences in isotopic ratio. Magma mixing is a potentially relevant, even likely process, but is unfortunately currently unconstrained in the system that is the subject of this study. Further work on isotopically distinct apatite cores may yield some insights into compositions of potential magma mixing components (see Section 5.4).

Finding #3: In all cases in which within-grain isotopic variations are observed, rims have lower isotopic ratios than cores. This result places an important constraint on viable degassing models that could be permissible with the presented observations. Systems that are strongly oxidizing and have melts that are dominated by sulfate can only concentrate ^{34}S in residual melts and therefore drive them to progressively higher isotopic ratios, the opposite of the trend observed. This is evident from both a modeling (Marini et al., 2011, Fig. 21) and an experimental perspective (Fiege et al., 2014, Fig. 2).

Finding #4: Sulfur concentration and $\delta^{34}S_{(CDT)}$ are positively correlated both in the core-rim pairs of individual crystals and in the overall trend of grain rims collectively. The concentration effect of S removal from the melt by the crystallization of apatite itself is minor relative to other effects, due to the low volumetric abundance of apatite (typically <1%) and to the trace concentrations of S in apatite observed in this system. Sulfur concentration variations imparted on the magma by apatite were an order of magnitude less than those observed.

Several synchronous complementary and competing processes effect the S concentration of crystallizing apatites. Decreasing S melt solubility (e.g. Clemente et al., 2004) and decreasing sulfate partitioning into apatite (e.g. Parat and Holtz, 2004) are both likely occurring during ascent and crystallization. These effects are possibly layered over decreasing bulk S concentration during degassing. Therefore, it is generally not surprising that apatites in this study record a drop in S concentration from core to rim. However, it is difficult to interpret the relative importance of these processes in determining the S concentration in apatite, as recognized by other workers (Peng et al., 1997; Streck and Dilles, 1998). And again, due to the preference for sulfate over sulfide in apatite, any fO$_2$ changes will result in significant changes in the availability of sulfate for partitioning into apatite.

Since no sulfate or sulfide phase was thus-far identified in these rocks, we have no direct information about whether S-bearing phases played a role in the concentration or isotope evolution preserved by these apatite crystals. The crystallization of sulfide, in concert with degassing, is modeled by Marini et al. (2011) demonstrating isotopic fractionations of the appropriate magnitude are possible. However, they demonstrate a negative correlation between melt S content and isotopic ratio produced by open-system sulfide precipitation, the opposite of that observed in apatite rims in this study, although variations between cores of different crystals could be related to such a process. It is notable that the co-variation between S concentration and S isotopic ratios is the opposite of that observed by Mandeville et al. (2009) for the Crater Lake system, likely due to the observed activity of sulfide in that system versus the possible lack of sulfide crystallization in Cadiz Valley Batholith magmas.

Anhydrite, a sulfate mineral, preferentially partitions ^{34}S over ^{32}S. In a melt with mixed-valence S speciation, anhydrite will crystallize with high S isotopic ratios and drive residual melt to lower sulfate concentrations and lower $\delta^{34}S_{(CDT)}$, consistent with the behavior observed in our specimens. Apatites with high S concentration cores have been observed in anhydrite-bearing systems (e.g. Streck and Dilles, 1998; van Hoose et al., 2013). Although none was observed in the system described here, anhydrite crystallization cannot be excluded as a viable explanation for the generation of observed isotopic and concentration variations.

5.2. Interpretations of Apatite Core and Rim Variations

5.2.1. High S concentration cores

Cores containing high S concentrations (from 0.3 to 0.65 wt.% SO$_3$) and isotopic ratios up to 3.8‰ higher than crystal rims are present in ~1 of every 10–12 apatites. Although not volumetrically dominant, these cores appear to record unique information about the early S behaviors of these samples. Possible genetic interpretations of apatite core origins include: 1. inheritance from pulses of magma with higher bulk δ^{34}S (Fig. 4); 2. inheritance from pulses of magma with more reduced fO$_2$ (Fig. 4); 3. inheritance from source or host rocks unrelated to magmatism; or 4. a record of early stages of crystallization when sulfate was more readily available to partition into apatite or partition coefficients were higher due to higher temperatures (Parat and Holtz, 2005). Cores could be potentially genetically related by sulfide fractionation, as modeled by Marini et al. (2011, Fig. 27). Textural interpretations can give qualitative information. Cores that record more moderate S concentrations (756-18 and 760-50) display zoning that oscillates between low concentration and moderate concentration, akin to the oscillatory zoning that is well-characterized in other minerals such as plagioclase feldspar and zircon (e.g. Shore and Fowler, 1996). This zoning could suggest that cores and zones in these grains are the product of crystallization-driven compositional changes and these cores could tentatively be fitted to the same degassing trajectory as apatite rims.

Conversely, the highest concentration cores have sharp boundaries, well-defined crystal faces and steep drops to low S concentrations. These characteristics are more suggestive of introduction of foreign crystals into an apatite-saturated magma and are generally inconsistent with a degassing trend. However, due to a lack of definitive evidence into the origin of high S concentration cores, only rim analyses are considered in modeling (see Section 5.3). But based on these lines of reasoning, we suggest that the cores from grains 756-76, 756-38, 756-35 and 756-95 are likely inherited, either from magma mixing or from source

rocks. Local sediments are Paleoproterozoic to Mesoproterozoic and are likely to have high isotopic ratios (Strauss, 1997); coupled assimilation-fractional crystallization processes would therefore yield an isotopic variation inconsistent with the one recorded during apatite crystallization. Alternatively, recharging, partially crystallized magmas containing apatite in their crystal cargoes may have been injected into an evolving magmatic system, or crystallized during S release events from injected mafic magmas as proposed by Edmonds et al. (2010) and Van Hoose et al. (2013) for Pinatubo. Considering the wide range of possible sources of these cores, it is not surprising that they do not yield a coherent geochemical story. Further exploration of these interpretations via trace elements and isotopic characteristics is the topic of ongoing research.

5.2.2. Low S concentration rims

Most mounted apatites were surveyed by two to five electron microprobe spots in order to identify high S concentration cores. This survey showed that ~90% of the apatite crystals from samples 756 and 760 had S concentrations below 0.2 wt.% SO_3. We therefore consider the low S concentration apatite rims to represent a sampling of the main stage of apatite crystallization. The first-order result from this study is that a 6‰ $\delta^{34}S$ isotopic variation was observed among the low-S rims of apatites from a single hand sample, and that this isotopic shift must have occurred during apatite crystallization. Although there is significant variation in the duration over which apatite will crystallize based on magma compositional parameters (Harrison and Watson, 1984; Piccoli and Candela, 2002), it is clear that a significant evolution of S systematics occurred during apatite crystallization in this system. Each particular apatite may crystallize only during a short window of this trajectory, especially if that crystal becomes included in another mineral. This is similar to the record preserved by melt inclusions that become trapped in progressively crystallizing minerals, as opposed to the record in volcanic matrix glasses, which are much closer to a representation of homogenized melt composition.

Reduction and oxidation degassing are open-system processes that exert a strong influence on fO_2, isotopic and bulk S characteristics of magmas. A significant proportion of S can be degassed at pressures at which the studied magmas were emplaced, ~150 MPa (Fiege et al., 2014). Sulfur degassing will decrease the bulk S concentration of the magma and have an impact on its isotopic ratio. As discussed above, degassing can produce isotopic fractionations towards either higher or lower $\delta^{34}S$, depending on the fO_2 of the melt, which determines what species will degas. The progression from higher to lower isotopic ratios with falling S from cores to rims, or the overall correlation between S concentration and $\delta^{34}S_{(CDT)}$, could be consistent with degassing of a mixed-valence gas species from a magma that is reduced enough to contain a significant proportion of dissolved sulfide. In experimental studies this occurred at fO_2 of NNO+1 or less, which falls squarely within the range over which natural and experimental melts demonstrate a mixed-valence environment in melts (e.g. Moretti et al., 2003; Moretti and Papale, 2004).

Following these lines of reasoning, we propose that degassing is a strong candidate to explain the concentration and isotopic ratio trajectories of the low S rims of apatites from this study in aggregate and explore it further.

5.3. Degassing modeling

Fig. 5 shows the results of combining experimentally constrained isotopic fractionations (Fiege et al., 2014) with a decompression degassing model (Burgisser et al., 2015). Isothermal decompression of a rhyolitic melt was modeled at 850 °C between 300 MPa and ~150 MPa as a function of the fraction of S lost by the melt (S melt content at the pressure of interest divided by the initial S melt content). The conditions are typical of wet cold felsic systems and are a reasonable approximation of those prevailing in the Cadiz Valley Batholith based on the mineralogy of these samples and compositions of Cretaceous arc magmas in general.

D-Compress calculates the molar fractions, m_i, of fluid species i, where i is one of H_2O, O_2, H_2, SO_2, S_2, H_2S, CO, CO_2, and CH_4. By assuming that chemical reactions are buffered by the fluid phase, it uses the fluid species fugacities, f_i, to calculate the weight fraction, w_i, of dissolved species due to a solubility law of the form $w_i = a_i f_i^{b_i}$, where a_i and b_i are constants depending on the species, i, and temperature (Burgisser et al., 2015). The H_2S/SO_2 fractions in the fluid and melt phases produced by D-Compress were then used to calculate the normalized fractions of SO_2 and H_2S in the fluid, R_{SO2g} and R_{H2Sg}, and melt, R_{SO2m} and R_{H2Sm}, phases according to:

$$R_{SO2g} = \frac{m_{SO2}}{m_{SO2} + m_{H2S}} \tag{1}$$

$$R_{H2Sg} = 1 - R_{SO2g} \tag{2}$$

$$R_{SO2m} = \frac{w_{SO2}}{w_{SO2} + \frac{64}{34} w_{H2S}} \tag{3}$$

$$R_{H2Sm} = 1 - R_{SO2m} \tag{4}$$

The melt S isotopic composition, $\delta^{34}S_m$, was calculated based on experimentally determined isotopic fractionation factors (Fiege et al., 2014), and following Sakai and Nagasawa (1958), Sakai et al. (1982):

$$\delta^{34}S_m = (\delta^{34}S_{init} + 10^3)(1 - w_{Smlost})^{\alpha_{g-m}-1} - 10^3 \tag{5}$$

with

$$\alpha_{g-m} = \alpha_1 \min(R_{SO2g}, R_{SO2m}) + \alpha_2 \min(R_{H2Sg}, R_{H2Sm})$$
$$+ \alpha_3 \max(0, R_{H2Sg} - R_{H2Sm}) + \alpha_4 \max(0, R_{SO2g} - R_{SO2m}) \tag{6}$$

where $\delta^{34}S_{init}$ is the initial value of $\delta^{34}S_m$, w_{Smlost} is the lost weight fraction of S in the melt, $\min(a, b)$ is a function returning the smallest of a and b, $\max(a, b)$ is a function returning the largest of a and b, $\alpha_1 = 0.9985$ is the fractionation coefficient between gaseous SO_2 and dissolved SO_2, $\alpha_2 = 1.0067$ is the fractionation coefficient between gaseous H_2S and dissolved H_2S, $\alpha_3 = 0.9949$ is the fractionation coefficient between gaseous H_2S and dissolved SO_2, and $\alpha_4 = 1.0103$ is the fractionation coefficient between gaseous
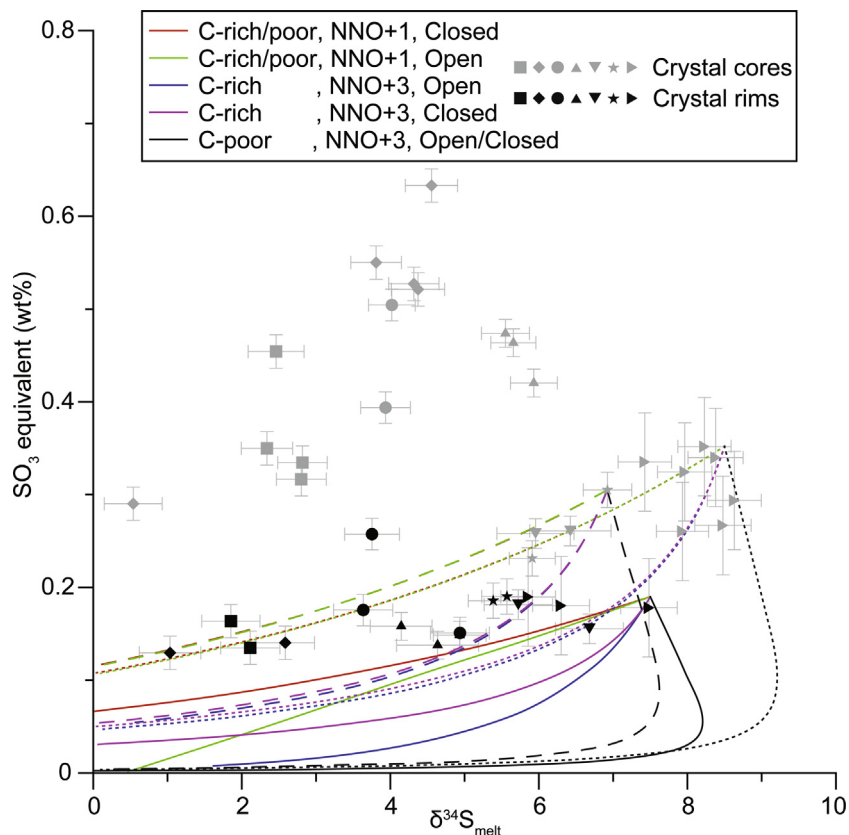
Fig. 5. Isotopic evolution of a rhyolitic melt decompressed between 300 MPa and ~150 MPa as a function of the fraction of sulfur lost by the melt. All runs were carried out at 850 °C and with 6.5 wt.% melt H_2O initially. Decompressions are either in closed (dashed curves) or open (continuous curves) system. Tick marks along the curves mark successively the 180 and 160 MPa isobars. Closed-system decompressions have 0.1 wt.% initial gas. Not all open-system decompressions reach 150 MPa because one species (generally CO_2) may be fully degassed out of the system before 150 MPa. Three starting redox states are simulated, and labels "CO_2 poor" mean 250 ppm initial melt CO_2 and labels "CO_2 rich" mean 1200 ppm initial melt CO_2. The most reduced runs (NNO+1) give identical results, regardless of initial CO_2 content. The gray area marks the uncertainty linked with the NNO+1, closed-system run.

SO_2 and dissolved H_2S. The melt weight fraction of S at a given pressure is $w_S = 0.5 w_{SO2} + 32/34 w_{H2S}$ and w_{Smlost} is:

$$w_{Smlost} = \frac{w_{Sinit} - w_S}{w_{Sinit}}$$

where w_{Sinit} is the S melt content at the initial pressure. To display the degassing trend in the same units as the data, w_{Smlost} is converted in SO_3 equivalent, SO_{3equ}, by using:

$$SO_{3equ} = SO_{3init}(1 - w_{Smlost}) \tag{7}$$

where SO_{3init} is the initial value of S apatite content (see Table 1). Eq. (7) assumes a linear relationship between the S content in the melt and the S content in the apatite.

Initial melt H_2O content was varied from 5 to 6.5 wt.%, initial pressure was varied from 200 to 300 MPa, and the initial gas content for closed-system decompression was varied from 10^{-5} to 2 wt.% without much effect on the behavior of melt $\delta^{34}S_{(CDT)}$ values ($\delta^{34}S_m$). The initial redox state, the initial melt CO_2 concentration, and the degassing style are the three main controls on the behavior of $\delta^{34}S_m$, so only the runs starting at 200 MPa, 5 wt.% melt H_2O, and 0.1 wt.% initial gas are presented. The three groups of five runs shown in Fig. 5 cover the ranges of initial variables

that yield the greatest span of $\delta^{34}S_m$. Not all open-system decompressions reach 150 MPa because the melt may run out of one species (generally CO_2) before that final pressure. Oxidized runs ($\geq$NNO+3) have nearly constant $\delta^{34}S_m$, regardless of melt CO_2 content or decompression style. Reduced runs ($\leq$NNO+1), on the other hand, show the largest $\delta^{34}S_m$ variations of each respective degassing style, regardless of melt CO_2 content. Overall, open-system degassing yields larger $\delta^{34}S_m$ variations than closed system degassing, but the effect of degassing style is subordinate to that of the redox state.

The models in Fig. 5 are run from three possible starting points that represent different interpretations of magmatic processes. One group of runs (solid lines) progresses from the highest measured rim $\delta^{34}S$ value from sample 756, which represents the assumption that all cores are foreign to the magma. Another group (dashed lines) progresses from the highest $\delta^{34}S$ measured in an oscillatory zoned core from sample 756, assuming that only discordant cores are foreign to this magma. The third group (dotted lines) progresses from the highest $\delta^{34}S$ value of the core of grain 760, assuming that samples 756 and 760 represent a shared magmatic history.

This modeling reproduces well the shallow slope of the small reduction in S concentration with significant isotopic variation observed in rims and oscillatory-zoned cores. It also reproduces the magnitude of isotopic ratio variation over a similar range in relative S concentration as that observed. These model curves do not lie directly over the data, possibly because the true composition at degassing initiation was not captured by our sampling, or because degassing initiated before apatite crystallization. Regardless of this limitation, we argue that this modeling captures the major first-order characteristics of the apatite rim data.

We favor an interpretation that the S and fO_2 systematics of this system, particularly represented by apatite rims, were dominated by ascent-driven degassing under conditions of ~NNO+1. This is well within the fO_2 range of estimates for the transition between sulfate-dominated and sulfide-dominated melts and the range in which apatites should still integrate dominantly sulfate according to Konecke et al. (2017), as is observed for these apatites (E. A.). Magma mixing (and/or assimilation) is a possible yet currently unquantified process that may influence apatite cores and the crystallization of anhydrite is also a possible explanation, although no anhydrite was observed in these samples. While these preliminary interpretations are speculative, they parallel the level of complexity that we have come to expect from magmatic systems, particularly intrusive ones. Although the system that is the topic of this study is incompletely constrained, the data suggest that records of multiple, discernable open-system processes are likely preserved in apatite crystals. The combination of these observations and the fine scale and relative chronology of this record makes it an excellent fit for comparison with more complex models.

5.4. Future work

The results of this study suggest several future avenues of research. The possibilites of melt-apatite isotopic fractionation for individual S species must be characterized in order to calculate true absolute melt sulfate isotopic ratios from isotopic ratios measured in apatite. There could be a systematic isotopic fractionation that, while unlikely to be of the magnitude observed, might be significant. Comparison of isotopic variations with a detailed study of S speciation in apatite is also likely to yield important additional insights.

The zoning record preserved in the studied crystals is actually much more detailed than can be accessed with traditional SIMS methods. Zoning on the scale of 1–2 μm cannot be interrogated with the relatively large (15–20 μm) spot sizes used here, but continued technical improvement in ion microscopy may allow for the quantification of these variations in greater detail. It is also notable that relative timing is discussed in this study, but no absolute time implication is presented. Crystallization may progress very rapidly or may experience lulls. Future work will include exploring strategies for absolute chronology, possibly using zircon inclusions and their trace elements (Dilles et al., 2015), as well as investigating in-situ trace elements and radiogenic isotopes such as Nd and Sr in these grains (e.g. Braund et al., 2017; Boehnke et al., 2017).

The S cycle influences the movement of economically valuable elements in the deep and shallow crust (see Rye and Ohmoto, 1974 and Simon and Ripley, 2011 for reviews). There are also many unresolved questions about redox systematics of magmatic arcs, particularly whether arc processes have an overall oxidizing effect on magmatic products (Carmichael, 1991; Lee et al., 2005; Rowe et al., 2009; Evans et al., 2012), how fO_2 and S systematics evolve in sub-volcanic magma systems (Mandeville et al., 2009; Oppenheimer et al., 2011; Moussallam et al., 2014) and how arc fO_2 evolution has impacted atmospheric evolution through geologic time (Canil et al., 2006). Constraining the processes that lead to arc magma oxidation has implications for the global fO_2 evolution of the earth (Saal et al., 2002; Canil et al., 2006; Dauphas et al., 2009). Due to the broad stability range of apatite, it is nearly ubiquitous in arc settings, including deep crustal xenoliths (Hanchar et al., 1994). The method presented here provides access to a unique record of magma S systematics on a scale that is correlative with the systematic complexity, and is a novel tool for addressing these important problems.

5.5. Conclusions

In this study, we present the first in-situ method of analyzing S isotopic ratios in apatite crystals. Sulfur isotopic fractionations of up to 6‰ $\delta^{34}S$ were observed in apatites from a single hand sample, and up to 3.8‰ $\delta^{34}S$ variations were observed within a single crystal. We combine these measurements with detailed S concentration maps in order to interpret potential systematic S behaviors. We favor an interpretation of these observations as a record of open system magmatic processes of degassing and mixing (or assimilation), and the crystallization of anhydrite remains a possible explanation. Preliminary degassing modeling reproduces the first-order characteristics of isotopic and concentration variation, including the magnitude and direction of isotopic fractionation. It further suggests an initial magma fO_2 of NNO+1 or lower, and that magmas were slightly reduced further through the process of degassing. More complex models that include both degassing and crystallization of solid S-bearing species, and their combined effect on the speciation of S and its isotopic fractionations will improve future constraints and interpretations of this and similar data sets. We argue that apatite is a high-fidelity recorder of the isotopic composition of the sulfate fraction, and possibly some sulfite and/or sulfide component, of a melt, and is a unique and critical new record for interpreting the behavior of S in magmas. We anticipate that, with further refinement, this method will yield valuable contributions to our understanding of complex, non-linear behaviors of S in magmas.

AUTHOR CONTRIBUTIONS

Contributions to the manuscript of first-author Economos include: project design, identification of the main science question, sample preparation, analytical design, interpretation of results, consultation on modeling and manuscript writing. Contributions of second author Boehnke include: data collection, interpretation of results and consultation during manuscript writing. Contributions of third author Burgisser include: degassing modeling, interpretation of comparison between models and results, and contributions to the text.

APPENDIX A. SUPPLEMENTARY MATERIAL

Supplementary data associated with this article can be found, in the online version, at http://dx.doi.org/10.1016/j.gca.2017.08.015.

REFERENCES

Anderson J. L. (1998) Core complexes of the Mojave-Sonoran desert: conditions of plutonism, mylonitization and decompression. In *Metamorphism and Crustal Evolution of the Western United States* (ed. W. Ernst). Prentice Hall, Englewood Cliffs, NJ, pp. 503–525.

Baker D. R. and Moretti R. (2011) Modeling the solubility of sulfur in magmas: a 50-year old geochemical challenge. *Rev. Mineral. Geochem.* **73**, 167–213.

Barboni M., Boehnke P., Schmitt A. K., Harrison T. M., Shane P., Bouvier A.-S. and Baumgartner K. (2016) Warm storage for arc magmas. *Proc. Natl. Acad. Sci.* **113**(49), 13959–13964.

Barth A. P. and Dorais M. J. (2000) Magmatic anhydrite in granitic rocks: first occurrence and potential petrologic consequences. *Am. Mineral.* **85**, 430–435.

Barth A. P., Wooden J. L., Jacobsen C. E. and Probst K. (2004) U-Pb geochronology and geochemistry of the McCoy Mountains formation, southeastern California: a Cretaceous retroarc foreland basin. *Geol. Soc. Am. Bull.* **116**, 142–153.

Barth A. P., Wooden J. L., Jacobsen C. E. and Economos R. C. (2013) Detrital zircon as a proxy for tracking the magmatic arc system: the California arc example. *Geology* **41**, 223–226.

Bateman P. C. and Chappell B. W. (1979) Crystallization, fractionation and solidification of the Tuolumne Intrusive Series, Yosemite National Park, California. *Geol. Soc. Am. Bull.* **90**, 465–482.

Beaudoin G., Taylor B. E., Rumble D. and Thiemens M. (1994) Variations in the sulfur isotope composition of troilite from the Canyon Diablo iron meteorite. *Geochim. Cosmochim. Acta* **58**, 4253–4255.

Beaudry P., Longpre M. -A., Economos R. C., Wing B., Bui T. -H., Stix J. (2015) Sulphur isotope systematics in sulphides and glasses from El Hierro, Canary Islands, Goldschmidt Annual Meeting, August, 2015.

Bindeman I. N. and Valley J. W. (2001) Low $\delta18O$ rhyolites from Yellowstone: magmatic evolution based on analyses of zircons and individual phenocrysts. *J. Petrol.* **40**, 1491–1517.

Boehnke P., Bell E. A., Trappitsch R., Stephan T., Pardo O. S., Davis A. M., Harrison T. M. (2017) Progress towards establishing early earth's crustal Rb/Sr ratio. Lunar and Planetary Science XLVII, abstract 2053.

Boyce J. W., Liu Y., Rossman G. R., Guan Y.-b., Eiler J. M., Stolper E. M. and Taylor L. A. (2010) Lunar apatite with terrestrial volatile abundances. *Nature* **466**, 466–469.

Braund E., Fowler M., Storey C. and Darling J. (2017) Apatite trace element and isotope applications to petrogenesis and provenance. *Amer. Mineral.* **102**, 75–84.

Burgisser A. and Scaillet B. (2007) Redox evolution of a degassing magma rising to the surface. *Nature* **445**, 194–197.

Burgisser A., Alletti M. and Scaillet B. (2015) Simulating the behavior of volatiles belonging to the C-O–H–S system in silicate melts under magmatic conditions with the software D-Compress. *Comp. Geosci.* **79**, 1–14.

Canil D., Johnston S. and Mihalynuk M. (2006) Mantle redox in Cordilleran ophiolites as a record of oxygen fugacity during partial melting and the lifetime of the mantle lithosphere. *Earth Planet. Sci. Lett.* **248**, 106–117.

Carmichael I. S. E. (1991) Redox of basic and silicic magmas: a reflection of their source regions? *Contrib. Mineral. Petrol.* **106**, 129–141.

Carroll M. and Rutherford M. J. (1987) The stability of igneous anhydrite: experimental results and implications for sulfur behavior in the 1982 El Chichon trachyandesite and other evolved magmas. *J. Petrol.* **28**, 781–801.

Carroll M. and Rutherford M. J. (1988) Sulfur speciation in hydrous experimental glasses of varying oxidation state – results from measured wavelength shifts of sulfur X-rays. *Am. Mineral.* **73**, 845–849.

Chambefort I., Dilles J. H. and Kent A. J. R. (2008) Anhydrite-bearing andesite and dacite as a source for sulfur in magmatic-hydrothermal mineral deposits. *Geology* **36**, 719–722.

Clemente B., Scaillet B. and Pichivant M. (2004) The solubility of S in hydrous silicate melts. *J. Petrol.* **45**, 2171–2196.

Coleman D. S. and Glazner A. F. (1997) The Sierra Crest magmatic event: rapid formation of juvenile crust during the Late Cretaceous in California. *Int. Geol. Rev.* **39**, 768–787.

Cooper K. M. and Kent A. J. R. (2014) Rapid remobilization of magma crystals kept in cold storage. *Nature* **506**, 480–483.

Cottrell E. and Kelley K. A. (2011) The oxidation state of Fe in MORB glasses and the oxygen fugacity of the upper mantle. *Earth Planet. Sci. Lett.* **305**, 270–282.

Dauphas N., Craddock P., Asimow P., Bennett V., Nutman A. and Ohnenstetter D. (2009) Iron isotopes may reveal the redox conditions of mantle melting from Archean to present. *Earth Planet. Sci. Lett.* **288**, 255–267.

Deering C. D., Gravley D. M., Vogel T. A., Cole J. W. and Leonard G. S. (2010) Origins of cold-wet-oxidizing to hot-dry-reducing rhyolite magma cycles and distribution in the Taupo Volcanic Zone, New Zealand. *Contrib. Mineral. Petrol.* **160**, 609–629.

Dilles J. H., Kent A. J., Wooden J. L., Tosdal R. M., Koleszar A., Lee R. G. and Farmer L. P. (2015) Zircon compositional evidence for sulfur-degassing from ore-forming arc magmas. *Soc. Econ. Geol. Sci. Commun.* **110**, 241–251.

Ding T., Valkiers S., Kipphardt H., De Bièvre P., Taylor P. D. P., Gonfiantini R. and Krouse R. (2001) Calibrated sulfur isotope

abundance ratios of three IAEA sulfur isotope reference materials and V-CDT with a reassessment of the atomic weight of sulfur. *Geochim. Cosmochim. Acta* **65**, 2433–2437.

Ducea M. N., McInnes B. I. A. and Wyllie P. J. (1994) Sulfur variations in glasses from volcanic rocks: effect of melt composition on sulfur solubility. *Int. Geol. Rev.* **36**, 703–714.

Ducea M. N., McInnes B. I. A. and Wyllie P. J. (1999) Experimental determination of compositional dependence of hydrous silicate melts on sulfate solubility. *Eur. J. Mineral.* **11**, 33–43.

Economos R. C., Barth A. P., Wooden J. L., Chapman A. D. (2011) Garnet formation and evolution in Cordilleran source rocks: inherited zircon trace element chemistry from the Transverse Ranges. *AGU Fall Meeting Abstract* #T53A-2485.

Edmonds M., Aiuppa A., Humphreys M., Moretti R., Giudice G., Martin R. S., Herd R. A. and Christopher T. (2010) Excess volatiles supplied by mingling of mafic magma at an andesite arc volcano. *Geochem. Geophys. Geosys.* **11**, Q04005. http://dx.doi.org/10.1029/2009GC002781.

Evans K., Elburg M. and Kamenetsky V. (2012) Oxidation state of subarc mantle. *Geology* **40**, 783–786.

Farquhar J., Jackson T. and Thiemens M. (2002) A 33S enrichment in ureilite meteorites: evidence for a nebular sulphur component. *Geochim. Cosmochim. Acta* **64**, 1819–1825.

Fiege A., Holtz F., Shimizu N., Mandeville C. W., Behrens H. and Knipping J. L. (2014) Sulfur isotope fractionation between fluid and andesitic melt: an experimental study. *Geochim. Cosmochim. Acta* **142**, 501–521.

Hanchar J. M., Miller C. F., Wooden J. L., Bennett V. C. and Staude J.-M. G. (1994) Evidence from xenoliths for a dynamic lower crust, Eastern Mojave Desert, California. *J. Petrol.* **35**, 1377–1415.

Harrison A. and Thode H. (1957) The kinetic isotope effect in the chemical reduction of sulphate. *Trans. Faraday. Soc.* **53**, 1648–1651.

Harrison T. M. and Watson E. (1984) The behavior of apatite during crustal anatexis: equilibrium and kinetic considerations. *Geochim. Cosmochim. Acta* **48**, 1467–1477.

Howard K. (2002) Geologic map of the Sheep Hole quadrangle, San Bernardino and Riverside counties, CA. USGS MF-2344.

Jugo P. J., Luth R. and Richards J. (2005) Experimental data on the speciation of S as a function of oxygen fugacity in basaltic melts. *Geochim. Cosmochim. Acta* **69**, 497–503.

Jugo P. J. (2009) Sulfur content at sulfide saturation in oxidized magmas. *Geology* **37**, 415–418.

Jugo P. J., Wilke M. and Botcharnikov R. E. (2010) Sulfur K-edge XANES analysis of natural and synthetic basaltic glasses: implications for S speciation and S content as a function of oxygen fugacity. *Geochim. Cosmochim. Acta* **74**, 5926–5938.

Kistler R. W., Chappell B. W., Peck D. L. and Bateman P. C. (1986) Isotopic variation in the Tuolumne Intrusive Suite, central Sierra Nevada, California. *Contrib. Mineral. Petrol.* **94**, 205–220.

Klimm K., Kohn S. C. and Botcharnikov R. E. (2012) The dissolution mechanism of S in hydrous silicate melts. II: Solubility and speciation of sulfur in hydrous silicate melts as a function of $f\mathrm{O}_2$. *Chem. Geol.* **322**, 237–249.

Konecke B. A., Fiege A., Simon A. C., Parat F. and Stechern A. (2017) Co-variability of S^{6+}, S^{4+} and S^{2-} in apatite as a function of oxidation state: implications for a new oxybarometer. *Am. Mineral.* **102**, 548–557.

Lee C.-T. A., Leeman W. P., Canil D. and Li Z. X. A. (2005) Similar V/Sc systematics in MORB and arc basalts: implications for the oxygen fugacites of their mantle source regions. *J. Petrol.* **46**, 2313–2336.

Li Y. and Liu J. (2006) Calculation of sulfur isotope fractionation in sulfides. *Geochim. Cosmochim. Acta.* **70**, 1789–1795.

Liu Y., Samaha N.-T. and Baker D. R. (2007) Sulfur concentration at sulfide saturation (SCSS) in magmatic silicate melts. *Geochim. Cosmochim. Acta* **71**, 1783–1799.

Mandeville C. W., Webster J. D., Tappen C., Taylor B. E., Timbal A., Sasaki A., Hauri E. and Bacon C. R. (2009) Stable isotope and petrologic evidence for open-system degassing during the climactic and pre-climactic eruptions of Mt. Mazama, Crater Lake, Oregon. *Geochim. Cosmochim. Acta* **73**, 2978–3012.

Marini L., Chiappini V., Cioni R., Cortecci G., Dinelli E., Principe C. and Ferrara G. (1998) Effect of degassing on sulfur contents and δ^{34}S values in Somma-Vesuvius magmas. *Bull. Volcanol.* **60**, 197-194.

Marini L., Moretti R. and Accornero M. (2011) Sulfur isotopes in magmatic-hydrothermal systems, melts and magmas. *Rev. Mineral. Geochem.* **73**, 423–491.

Métrich N., Berry A. J., O'Neill H., St C. and Susini J. (2009) The oxidation state of sulfur in synthetic and natural glasses determined by X-ray absorption spectroscopy. *Geochim. Cosmochim. Acta* **73**, 2382–2399.

Miller J., Matzel J., Miller C., Burgess S. and Miller R. (2007) Zircon growth and recycling during the assembly of large, composite arc plutons. *J. Volc. Geotherm. Res.* **176**, 282–299.

Miyoshi T., Sakai H. and Chiba H. (1984) Experimental study of sulfur isotope fractionation factors between sulfate and sulfide in high temperature melts. *Geochem. J.* **2**, 75–84.

Moore G. and Carmichael I. S. E. (1998) The hydrous phase equilibria (up to 3 kbar) of an andesite and basaltic andesite from western Mexico: constraints on water content and conditions of phenocryst growth. *Contrib. Mineral. Petrol.* **130**, 304–319.

Moretti R., Papale P., Ottonello G. (2003) A model for the saturation of C-H-O-S fluids in silicate melts. In Volcanic Degassing (eds. C. Oppenheimer, D. M. Pyle, J. Barclay). *Geol. Soc. London Spec. Pub.* 213, pp. 81–101.

Moretti R. and Papale P. (2004) On the oxidation state and volatile behavior in multicomponent gas-melt equilibria. *Chem. Geol.* **213**, 265–280.

Moretti R. and Baker D. R. (2008) Modeling the interplay of fO2 and fS2 along the FeS-silicate melt equilibrium. *Chem. Geol.* **256**, 286–298.

Moussallam Y., Oppenheimer C., Scaillet B., Gaillard F., Kyle P., Peters N., Hartley M., Berlo K. and Donovan A. (2014) Tracking the changing oxidation state of Erebus magmas, from mantle to surface, driven by magma ascent and degassing. *Earth Planet. Sci. Lett.* **393**, 200–209.

Ohmoto H. (1986) Stable isotope geochemistry of ore deposits. *Rev. Mineral. Geochem.* **16**.

Oppenheimer C., Moretti R., Kyle P. R., Eschenbacher A., Lowenstern J. B., Hervig R. L. and Dunbar N. (2011) Mantle to surface degassing of alkali magmas at Erebus volcano, Antarctica. *Earth Planet. Sci. Lett.* **306**, 261–271.

Parat F., Dungan M. and Streck M. J. (2002) Anhydrite, pyrrhotite and sulfur-rich apatite: tracing the sulfur evolution of an Oligocene andesite (Eagle Mountain, CO, USA). *Lithos* **64**, 63–75.

Parat F. and Holtz F. (2004) Sulfur partitioning between apatite and melt and effect of sulfur on apatite solubility at oxidizing conditions. *Contrib. Mineral. Petrol.* **147**, 201–212.

Parat F. and Holtz F. (2005) S partition coefficient between apatite and rhyolite: the role of bulk S content. *Contrib. Mineral. Petrol.* **150**, 643–651.

Parat F., Holtz F. and Streck M. J. (2011) Sulfur-bearing magmatic accessory minerals. *Rev. Mineral. Geochem.* **73**, 285–314.

Paterson S. R., Okaya D., Memeti V., Economos R. C. and Miller R. B. (2011) Magma addition and flux calculations of incrementally constructed magma chambers in continental margin arcs: combined field, geochronologic and thermal modeling studies. *Geosphere* **7**, 1439–1468.

Peng G., Luhr J. and McGee J. (1997) Factors controlling S concentrations in volcanic apatite. *Am. Mineral.* **82**, 1210–1224.

Piccoli P. M. and Candela P. A. (2002) Apatite in igneous systems. *Rev. Mineral. Geochem.* **48**, 255–292.

Pyle J. M., Spear F. S. and Wark D. A. (2002) Electron Microprobe analysis of REE in apatite, monazite and xenotime: protocols and Pitfalls. *Rev. Mineral. Geochem.* **48**, 1.

Richet P., Bottinga Y. and Javoy M. (1977) A review of hydrogen, carbon, nitrogen, sulfur and chlorine stable isotope fractionation among gaseous molecules. *An. Rev. Earth Planet. Sci.* **5**, 65–110.

Rowe M. C., Kent A. J. R. and Nielsen R. L. (2009) Subduction influence on oxygen fugacity and trace and volatile elements in basalts across the Cascade volcanic arc. *J. Petrol.* **50**, 61–91.

Rye R. O. and Ohmoto H. (1974) Sulfur and carbon isotopes in ore genesis: a review. *Econ. Geol.* **69**, 826–842.

Saal A. E., Hauri E. H., Langmuir C. H. and Perfit M. R. (2002) Vapour undersaturation in primitive mid-ocean-ridge basalts and the volatile content of the Earth's upper mantle. *Nature* **419**, 451–455.

Sakai H. and Nagasawa H. (1958) Fractionation of sulfur isotopes in volcanic gases. *Geochim. Cosmochim. Acta* **15**, 32–39.

Sakai H. (1968) Isotopic properties of sulfur compounds in hydrothermal processes. *Geochem. J.* **2**, 29–49.

Sakai H., Casadevall T. J. and Moore J. G. (1982) Chemistry and isotope ratios of sulfur and volcanic gasses at Kilauea Volcano, Hawaii. *Geochim. Cosmochim. Acta* **46**, 729–738.

Shore M. and Fowler A. D. (1996) Oscillatory zoning in minerals: a common phenomenon. *Can. Mineral.* **34**, 1111–1126.

Simon A. C. and Ripley E. M. (2011) The role of magmatic sulfur in the formation of ore deposits. *Rev. Mineral. Geochem.* **73**, 513–578.

Stock M. J., Humphreys M. C. S., Smith V. C., Isaia R. and Pyle D. M. (2015) Late-stage volatile saturation as a potential trigger for explosive volcanic eruptions. *Nat. Geosci.* **9**, 249–254.

Strauss H. (1997) The isotopic composition of sedimentary S through time. *Palaeo* **132**, 97–118.

Streck M. and Dilles J. (1998) Sulfur evolution of oxidized arc magmas as recorded in apatite from a porphyry copper batholith. *Geology* **26**, 523–526.

Tepper J. H. and Kuehner S. M. (1999) Complex zoning in apatite from the Idaho batholith: a record of magma mixing and intracrystalline trace element diffusion. *Am. Mineral.* **84**, 581–595.

Van Hoose A. E., Streck M. J., Pallister J. S. and Wälle M. (2013) Sulfur evolution of the 1991 Pinatubo magmas based on apatite. *J. Volc. Geotherm. Res.* **257**, 72–89.

Wallace P. and Carmichael I. S. E. (1992) Sulfur in basaltic magmas. *Geochim. Cosmochim. Acta* **56**, 1863–1874.

Wallace P. and Edmonds M. (2011) The S budget in magmas: evidence from melt inclusions, submarine glasses, and volcanic gas emissions. *Rev. Mineral. Geochem.* **73**, 215–246.

White S., Crisp J. and Spera F. (2006) Long-term volumetric eruption rates and magma budgets. *Geochem. Geophys. Geosyst*. http://dx.doi.org/10.1029/2005GC001002.

Associate Editor: Edward M. Ripley